Viscous Co-Current Downward Taylor Flow in a Square Mini-Channel

Özge Keskin
Institute of Science and Technology, University of Sakarya, TR-54187 Sakarya, Turkey
Forschungszentrum Karlsruhe, Institut für Reaktorsicherheit, Postfach 3640, D-76021 Karlsruhe, Germany

Martin Wörner
Forschungszentrum Karlsruhe, Institut für Kern- und Energietechnik, Postfach 3640, D-76021 Karlsruhe, Germany

Hakan S. Soyhan
Dept. of Mechanical Engineering, University of Sakarya, TR-54187 Sakarya, Turkey

Tobias Bauer
Dept. of Chemical Engineering, Technische Universität Dresden, D-01062 Dresden, Germany

Olaf Deutschmann
Forschungszentrum Karlsruhe, Institut für Kern- und Energietechnik, Postfach 3640, D-76021 Karlsruhe, Germany
Institute for Chemical Technology and Polymer Chemistry, Universität Karlsruhe, D-76128 Karlsruhe, Germany

Rüdiger Lange
Dept. of Chemical Engineering, Technische Universität Dresden, D-01062 Dresden, Germany

DOI 10.1002/aic.12113
Published online November 9, 2009 in Wiley InterScience (www.interscience.wiley.com).

This article presents a computational study of the co-current downward Taylor flow of gas bubbles in a viscous liquid within a square channel of 1 mm hydraulic diameter. The three-dimensional numerical simulations are performed with an in-house computer code, which is based on the volume-of-fluid method with interface reconstruction. The computed (always axi-symmetric) bubble shapes are validated by experimental flow visualizations for varying capillary number. The evaluation of the numerical results for a series of simulations reveals the dependence of the bubble diameter and the interfacial area per unit volume on the capillary number. Correlations between bubble velocity and total superficial velocity are also provided. The present results are useful to estimate the values of the bubble diameter, the liquid film thickness and the interfacial area per unit volume from given values of the gas and liquid superficial velocities. © 2009 American Institute of Chemical Engineers *AIChE J,* 56: 1693–1702, 2010
Keywords: Taylor flow, mini-channel, multiphase monolith reactor, interfacial area per unit volume, computational fluid dynamics

Correspondence concerning this article should be addressed to M. Wörner at martin.woerner@iket.fzk.de.

Introduction

The hydrodynamics of gas–liquid two-phase flow in narrow channels has attained increasing interest within the last

decade not only for nuclear reactors, power electronic devices, and compact heat exchangers but also for chemical multiphase reactors, such as monolithic reactors[1] and microstructured reactors.[2] While for the latter application channel dimensions are typically on the order of 100 μm, for heterogeneous catalyzed gas/liquid reactions channel dimensions are often on the order of 1 mm. Monolith reactors typically consist of parallel, straight mini-channels with square cross-section and with hydraulic diameters in the range of 0.5–3 mm. This size guarantees a reasonable balance between pressure drop and catalytic active area as well as mechanical stability. The most attractive gas/liquid flow regime for monolith reactors is Taylor flow because of the high gas/liquid and overall gas/liquid/solid mass transfer rates. The term Taylor flow was introduced by Irandoust and Andersson[3] and refers to a special case of slug flow where the bullet-shaped bubbles (Taylor bubbles[4]) are separated by liquid slugs with no gas entrained. There is only a thin liquid film between the elongated part of the gas bubble and the channel wall. Other designations frequently used in the literature for this type of flow are segmented flow and bubble train flow.

While on an industrial scale monolith reactors operated in Taylor flow are nowadays used, for example, for the production of hydrogen peroxide,[5] they have been proposed as a possible reactor for Fischer-Tropsch synthesis.[6,7] Recent measurements during Fischer-Tropsch synthesis showed enhanced reaction rates for a fixed-bed reactor with monolithic catalyst in the Taylor flow regime as compared to a stirred tank reactor with suspended powder catalyst.[8] Furthermore, higher C5–C18 liquid fractions are obtained by conducting the Fischer-Tropsch reaction in a monolith catalyst with straight flow channels rather than a packed-bed of catalyst particles.[9] These results are attributed to the advantageous mass transfer characteristics of the monolith reactor in the Taylor flow regime. Various aspects of gas–liquid two-phase flow in structured packings, monolith reactors, and mini-channels are discussed in recent review papers by Pangakar et al.,[10] Kreutzer et al.,[11] and Angeli and Gavriilidis.[12] According to the latter review, the hydrodynamics of developed Taylor flow in circular channels is largely understood while more information and predictive models are needed for noncircular channels.

From an ideal point of view, the Taylor flow should consist of bubbles of identical size and shape that move along the channel with the same axial velocity and are separated from each other by liquid slugs of uniform length. The hydrodynamics of such a uniform Taylor flow is fully described by a unit cell which consists of one gas bubble and one liquid slug. Uniform Taylor flow allows estimation of the behavior of a single channel as well as the entire multichannel reactor by numbering-up the relevant transport phenomena of the unit cell. In technical multichannel applications, however, uniform Taylor flow is hardly achieved, because the bubble generation often leads to a distribution of bubble sizes.[13]

For a better understanding of the basic hydrodynamic phenomena, experiments on Taylor flow are often performed in visually accessible single channels. Thulasidas et al.[14] determined relations for main mass transfer parameters such as bubble size and shape, bubble velocity, and volume fraction of the gas on the basis of the superficial flow rates of gas and liquid. They considered co-current upward Taylor flow inside capillaries of circular and square cross-section with hydraulic diameter of 2 mm. Recently, Tsoligkas et al.[15] investigated the differences between up-flow and down-flow hydrodynamics in a single channel. In their experiments, they considered the flow of water or an isopropanol/water mixture and air in square glass capillaries of 1.5 and 2 mm hydraulic diameter. In a follow-up study,[16] they found for a capillary reactor with circular cross-section and diameter 1.69 mm significantly higher liquid–solid mass transfer rates for up-flow compared with down-flow.

There exist a limited number of numerical studies on single Taylor bubbles or Taylor flow in small noncircular channels.[17–21] Commercial computational fluid dynamics (CFD) codes, which apply the volume-of-fluid (VOF) method for tracking the gas–liquid interface, are often used for numerical investigations. However, VOF methods without interface reconstruction have strong deficiencies,[22] and only VOF methods with geometric interface reconstruction give reliable and consistent results.[23] Many computational studies are difficult to be validated quantitatively by experiments. Often, validation is restricted to integral flow quantities as functions of the capillary number. Examples are the ratio between bubble velocity and total superficial velocity and the nondimensional relative bubble velocity. For the validation of computed bubble shapes often only the maximum diameter of axi-symmetric bubbles is available. In experiments, the data are usually obtained for a range of bubble and liquid slug lengths. An exact representation of the experiment in the computation is hardly possible, which allows qualitative comparison only.

This paper presents a combined experimental and numerical investigation of the co-current downward Taylor flow in a glass mini-channel having a square cross-section of 1 mm $\times$ 1 mm. The fluids considered are nitrogen as gas and squalane ($C_{30}H_{62}$) as continuous liquid phase. Squalane is a viscous liquid and as an inert species serves as good solvent for Fischer-Tropsch products.[8,24] In the experiments, the gas and liquid superficial velocities are in the ranges of 0.05–0.2 m/s and 0.017–0.1 m/s, respectively. High-speed video camera images are used to roughly estimate the axial length of a unit cell and the gas holdup within the unit cell. Based on these parameters, a series of transient three-dimensional numerical simulations with a VOF method are performed for two different values of the axial length of the unit cell and two different gas holdups within the unit cell. Comparisons of the experimentally obtained and computed gas bubble shapes serve as detailed validation of the numerical method and the in-house computer code. The numerical data are then used to analyze various flow quantities.

Experimental Section

A test system was designed for the investigation of the gas–liquid two-phase flow consisting of a capillary setup and an image recording setup. The downward gas–liquid two-phase flow was studied in a square mini-channel made of glass (Hilgenberg GmbH). The inner and outer dimensions of the square mini-channel were 1 mm $\times$ 1 mm and 1.65 mm $\times$ 1.65 mm, respectively. The length of the mini-channel was 300 mm, i.e., 300 times the hydraulic diameter. We assumed that this is sufficient for the flow to be fully

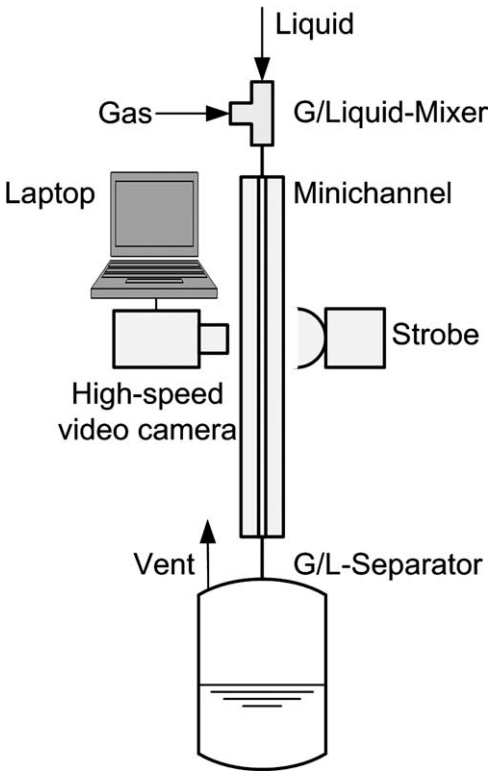

Figure 1. Simplified schematic diagram of the experimental set up.

developed after half of the length of the mini-channel. The mini-channel was embedded in transparent resin to enhance the mechanical strength and resistance to pressure. In test runs, the embedded mini-channel resisted pressure up to 60 bar; in this study, the experiments were performed at a pressure of 20 bar. A simplified schematic diagram of the experimental setup is given in Figure 1 (for a detailed version including the complete instrumentation, see Bauer[25]). The liquid was supplied from a tank and its flow rate was controlled by a high-performance liquid chromatography pump (Knauer, model: WellChrom K-1800). The gas was supplied from a compressed gas cylinder and the flow rate was adjusted by a mass flow controller (Brooks, model: 5850 E or Bronkhorst, model F-232M). The gas and liquid were mixed together in a V-shape micro-mixer [Forschungszentrum Karlsruhe (FZK), Institute for Micro Process Engineering]. The micro-mixer consists of 675 microchannels with cross-sections of 100 μm $\times$ 70 μm for each fluid passage. The pressure within the mini-channel was adjusted with an overflow valve and measured at the channel exit. The gas–liquid separator was used to recycle the liquid. Temperature indicators provided the inlet and outlet temperatures while micro heat exchangers could be used for experiments at elevated temperatures; in this study, all experiments were conducted at 25°C. In the event of failure, the operator and the apparatus were protected by check valves, nonreturn valves and a safety valve. Downward gas–liquid two-phase flow was visualized using a high-resolution high-speed video camera (VDS Vosskühler Gmbh, model: HCC 1000) placed at the center of the mini-channel. The high-speed camera system consists of a high-resolution CMOS camera, an IEEE1394 interface as well as control software for a PC under Windows. The image rate can be set at up to 462 frames per second (fps) with a resolution of 1024 $\times$ 1024 pixel or set up to 1825 fps with a resolution of 1024 $\times$ 256 pixel. Once recorded, the data are transferred from the camera memory to a laptop computer via an IEEE1394 interface. The images are stored on the PC in bitmap file format. The embedded mini-channel was illuminated stroboscopically (Elmed Messtechnik, model: 06100016) with an exposure time of 10 μs. The resolution adjusted was 1024 $\times$ 256 pixels with a pixel size of 13.75 μm $\times$ 13.75 μm for all experiments. A recorded image showed 14 mm of the mini-channel length.

The experiments were performed at a pressure of 20 bar for three different liquid superficial velocities (J_L = 0.017, 0.05, and 0.1 m/s) and for three different gas superficial velocities (J_G = 0.05, 0.1, and 0.2 m/s), resulting in nine different parameters sets. The total superficial velocity $J \equiv J_G + J_L$ was in the range of 0.067–0.3 m/s while the volumetric flow rate ratio $\beta \equiv J_G/J$ was in the range of 0.333–0.922. As shown in Figure 2a, Taylor flow occurred for all parameters studied. However, there exist considerable variations of the bubble length, the liquid slug length, and the unit cell length for the different flow parameters.

Numerical Simulation

Numerical method

The computations are performed with an in-house computer code, called TURBIT-VOF, which was developed at FZK. This code solves the Navier-Stokes equation with surface tension term in nondimensional single field formulation for two incompressible Newtonian fluids with constant

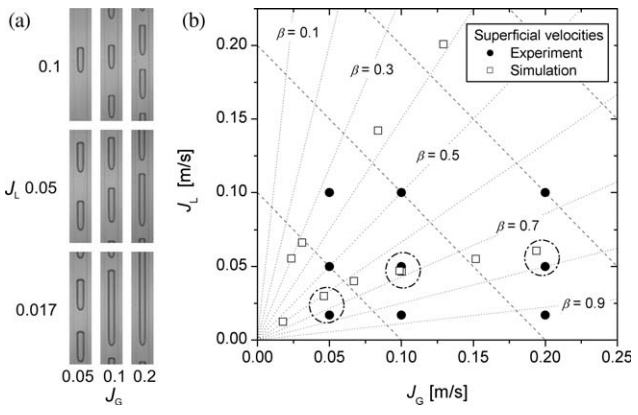

Figure 2. (a) Images with typical flow patterns for the different combinations of gas and liquid superficial velocity in the experiment (values of J_L and J_G are in m/s). (b) Superficial velocities J_L and J_G in experiment (filled circles) and simulation (open squares).

The dashed lines represent lines of constant $J = J_L + J_G$ while the dotted lines represent lines of constant $\beta = J_G/J$. The three dashed-dotted circles indicate experimental and numerical cases that are compared in Figure 3.

viscosity and coefficient of surface tension on a regular staggered Cartesian grid by a finite volume method. All spatial derivatives are approximated by central differences. Time integration is performed by an explicit third order Runge-Kutta method. A divergence free velocity field at the end of each time step is enforced by a projection method, in which the resulting Poisson equation is solved by a conjugate gradient technique. The dynamic evolution of the interface is computed by a VOF method with piecewise planar interface reconstruction. For further details about the governing equations and the numerical method we refer to Ghidersa et al.[17] and Öztaskin et al.[26]

Numerical and physical parameters

In this section, we present the computational set-up and the numerical and physical parameters for the simulations of co-current downward Taylor flow of squalane/nitrogen in a square vertical channel with inner side length $W = 1$ mm. As the physical properties of squalane at a pressure of 20 bar are not available to our knowledge, in the simulations the known properties at standard conditions are taken, which are $\rho_L = 802$ kg/m^3, $\mu_L = 0.029$ Pa s, and $\sigma = 0.0286$ N/m. Thus, the viscosity of squalane is about 30 times as much as that of water. For nitrogen at a pressure of 20 bar $\rho_G = 23.6$ kg/m^3 and $\mu_G = 0.01804$ mPa·s are used in the simulations. The ratio of hydraulic diameter to Laplace length, $\Lambda \equiv \sqrt{\sigma/(g(\rho_L - \rho_G))}$, is $D_h/\Lambda = 0.517$, which corresponds to an Eötvös number of $Eo \equiv (D_h/\Lambda)^2 = g(\rho_L - \rho_G)D_h^2/\sigma = 0.267$. These values indicate that gravitational effects may not be neglected in a millimeter size channel (see also Tsoligkas et al.[15]).

For the computational set-up, we follow the procedure of our previous papers[17,19] and consider one unit cell, which consists of one gas bubble and one liquid slug. We use in axial (vertical) direction periodic boundary conditions to mimic the influence of the trailing and leading bubble in Taylor flow. No-slip boundary conditions are applied at the four lateral walls of the square channel. There are two important parameters which have to be fixed in this set-up for any simulation run: the gas holdup in the unit cell (ε_G) and the axial length of the unit cell (L_{uc}). The latter length is given by the distance from the nose of one bubble to that of the next bubble. Figure 2a indicates a considerable variation of both, L_{uc} and ε_G in the experiment. As long unit cells are computationally expensive, we restrict the present study to two medium values of the unit cell length, namely $L_{uc}/W = 4$ and 6. These values are typical for values of β in the range of 0.5–0.8 in the experiments. We also consider two different values for the gas holdup, namely $\varepsilon_G = 0.2$ and 0.4. This results in four different combinations of both parameters.

For all cases, a uniform Cartesian grid consisting of cubic mesh cells was used, with y denoting the axial (vertical) direction and x and z the wall-normal directions. The mesh size h is determined as follows: A value for U_B was estimated from the experimental movies and the corresponding capillary number, $Ca \equiv \mu_L U_B/\sigma$, is computed. Then, based on Ca the bubble diameter D_B (i.e., the maximum bubble dimension in a horizontal direction) and the liquid film thickness $\delta_{LF} = (W - D_B)/2$ were estimated from the experimental results of Thulasidas et al.[14] (for upward flow). From our experience with previous simulations,[17,19,23] we know that about 3–4 mesh cells are at minimum required to resolve the liquid film. This yields a first estimate for h. In the present simulations, Ca is in the range of 0.045–0.66 and the values of D_B/W are in the range of 0.8–0.95. The thickness of the liquid film δ_{LF}/W is then in the range of 0.1–0.025. A grid size of $h/W \approx 0.03$–0.008 is therefore required to resolve the liquid film by three mesh cells. The higher value corresponds to a grid with 30×30 mesh cells per channel cross-section while the lower value requires 120×120 mesh cells. However, such a fine grid cannot be afforded if a series of simulations are to be performed. Therefore, as a compromise a grid size of $h/W = 1/80$ was chosen. For the small domain with nondimensional size $L_x/W \times L_y/W \times L_z/W = 1 \times 4 \times 1$ this resulted in a grid with $80 \times 320 \times 80$ mesh cells while for the large domain ($1 \times 6 \times 1$) a grid with $80 \times 480 \times 80$ mesh cells and thus about 3×10^6 mesh cells in total were used. Here, L_x, L_y, and L_z denote the dimensions of the computational domain. The time step width was constant for each case and in the range of 0.17–0.4 μs.

The initial phase distribution of the simulations was defined by placing an elongated axi-symmetric bubble of volume $V_B = \varepsilon_G L_x L_y L_z$ on the channel axis. The initial velocity field for both phases was given by fluids at rest, or, to save CPU time, by a constant axial velocity, or by a parabolic axial velocity profile within the channel cross-section (which was axially uniform). Starting from these initial conditions, the flow is driven by a constant source term in the axial momentum equation. This source term corresponds to the axial pressure drop along the unit cell. This two-phase pressure drop was not measured in the experiments. Therefore, for the simulations an estimated value was used, which accounts for the hydrostatic pressure difference and the pressure drop across the liquid slug but neglects the pressure drop along the bubble. In the transient simulations the evolution from the initial velocity field and prescribed bubble shape toward a fully developed Taylor flow was computed. Fully developed flow was assured by recording the mean axial gas and liquid velocities in the computational domain and continuing the simulation till both velocities approach constant terminal values. In the present paper, only these fully developed flow results and the corresponding computed steady bubble shapes are discussed. To save CPU time, for some cases a new transient simulation was started from an already fully developed case. For that purpose, the driving pressure gradient of the fully developed case was increased (or decreased) and the simulation was continued till constant terminal mean gas and liquid axial velocities were obtained again.

At this point, we note a distinct difference between the experiments and the simulations. In the experiments, the flow rates are specified and the unit cell length, the gas holdup and the pressure drop adjust accordingly. In contrast, in our simulations the length of the unit cell, the gas holdup, and the pressure drop were fixed and the flow rates adjust accordingly. While the present simulation set-up is convenient to computationally mimic Taylor flow, it makes a real 1:1 recalculation of certain experimental conditions difficult.

In Table 1, we list the parameters of all simulation runs and the resulting superficial gas and liquid velocities. The terminal values of the capillary and bubble Reynolds

Table 1. Overview on Parameters and Results of all Simulation Runs

Case	L_{uc}/W	ε_G	Δp (Pa)	J_L (m/s)	J_G (m/s)	β	Ca	Re_B	D_B/W	A_B/W^2
4_20_A	4	0.2	−199.5	0.0555	0.0236	0.299	0.120	3.26	0.931	4.43
4_20_B	4	0.2	−754.4	0.2008	0.1292	0.391	0.655	17.86	0.794	4.83
4_40_A	4	0.4	−199.5	0.0465	0.1002	0.683	0.254	6.93	0.880	8.37
4_40_B	4	0.4	−245.7	0.0551	0.1517	0.734	0.385	10.49	0.840	8.58
6_20_A	6	0.2	−337.8	0.0663	0.0310	0.319	0.157	4.29	0.904	6.29
6_20_B	6	0.2	−753.5	0.1421	0.0839	0.371	0.425	11.60	0.830	6.69
6_40_A	6	0.4	−62.6	0.0124	0.0177	0.588	0.045	1.22	0.953	11.48
6_40_B	6	0.4	−168.8	0.0299	0.0462	0.607	0.117	3.19	0.956	11.53
6_40_C	6	0.4	−230.6	0.0401	0.0671	0.626	0.170	4.64	0.945	11.69
6_40_D	6	0.4	−267.2	0.0456	0.0984	0.684	0.250	6.81	0.894	12.10
6_40_E	6	0.4	−373.8	0.0607	0.1938	0.762	0.491	13.40	0.827	12.62

For each case, the denotation is as follows: the first and second numbers indicate the nondimensional length of the unit cell L_{uc}/W and the gas holdup ε_G (in %), respectively, while the letter distinguishes cases with the same L_{uc}/W and ε_G but different prescribed pressure drop Δp.

numbers are given as well. Both are related in terms of $Re_B \equiv \rho_L D_h U_B/\mu_L = La{\cdot}Ca$, where $La \equiv \sigma\rho_L D_h/\mu_L^2$ is the Laplace number which is constant here ($La = 27.27$). In the numerical simulations, the capillary number was in the range of $0.045 \leq Ca \leq 0.66$ while the range of the bubble Reynolds number was $1.22 \leq Re_B \leq 17.9$. The range of the Weber number was $0.055 \leq We \leq 11.7$, where $We \equiv \rho_L D_h U_B^2/\sigma = Re_B{\cdot}Ca$. In a square channel, the bubble shape is axi-symmetric in any axial cross-section for $Ca > 0.04$. For $Ca < 0.04$ the bubble becomes nonaxisymmtric as it advances into the corners of the channel, as found numerically by Ratulowski and Chang[27] and confirmed experimentally for co-current upward flow by Thulasidas et al.[14] So, all present simulations correspond to the axi-symmetric bubble shape regime.

Results

In this section, we present and discuss the results of the experiments and numerical simulations. We are in particular interested in the influence of the capillary number on various quantities. First, the computed bubble shapes are compared with those from experiments and then relations between characteristic velocities of Taylor flow are considered.

Influence of capillary number on bubble shape

Figure 2b shows the different gas and liquid superficial velocities in the experiments and simulations. Three cases were identified, for which the combination (J_L, J_G) was similar in experiment and simulation; the corresponding experimental values are (0.017, 0.05 m/s), (0.05, 0.1 m/s), and (0.1, 0.2 m/s). In Figure 3, we compare the bubble shapes of these experiments with that obtained in simulations with $L_{uc} = 6$ mm for similar values of (J_L, J_G). Unfortunately, in the experimental images only the external wall border of the transparent mini-channel (1.65 mm) is visible, while the inner wall border (1 mm) cannot be recognized. In the numerical visualizations both, the inner and external wall borders of the mini-channel are indicated by lines. To allow for a reasonable visual comparison of the experimental and numerical images in Figure 3, the images are scaled by the external dimension of the mini-channel. Figure 3 shows that the change of the bubble shape, that is associated with an increase of the total superficial velocity in the experiment, is well reproduced by the numerical simulations. This agreement holds in particular for the shape of the bubble front and bubble back. In Figure 4 we compare the computed bubble shapes for all cases. Figures 3 and 4 show that with increasing value of Ca, the bubble front becomes more pointed while the bubble rear becomes more flat. These results are in agreement with those of Taha and Cui[18] who found that bubbles acquire spherical ends at low Ca, while the shape at the back of the bubbles changes from convex to concave at high Ca. This behavior is similar to that in circular channels[28] and was also found in equi-triangular capillaries.[20]

After this visual verification, we use the simulations to evaluate data that have not been measured, e.g., the bubble diameter and the interfacial area per unit volume. In Figure 5, we show the ratio D_B/W as function of the capillary number. It is well known[11,12] that the liquid film thickness increases with increasing Ca, hence the bubble diameter decreases. The numerical results in Figure 5 show that D_B/W depends not only on Ca but also on the bubble size. The latter can be

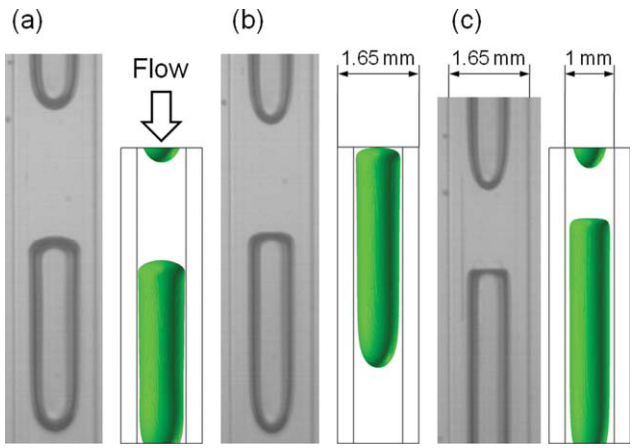

Figure 3. Comparison of bubble shape in experiment (left) and simulation (right) for similar liquid and gas superficial velocities.

(a) $(J_L,J_G)_{Exp}$ = (0.017, 0.05 m/s), $(J_L, J_G)_{Sim}$ = (0.03, 0.046 m/s) (case 6_40_ B); (b) $(J_L, J_G)_{Exp}$ = (0.05, 0.1 m/s), $(J_L, J_G)_{Sim}$ = (0.046, 0.098 m/s) (case 6_40_ D); (c) $(J_L, J_G)_{Exp}$ = (0.05, 0.2 m/s), $(J_L, J_G)_{Sim}$ = (0.061, 0.194 m/s) (case 6_40_ E). For case denotations see Table 1. [Color figure can be viewed in the online issue, which is available at www.interscience.wiley.com.]

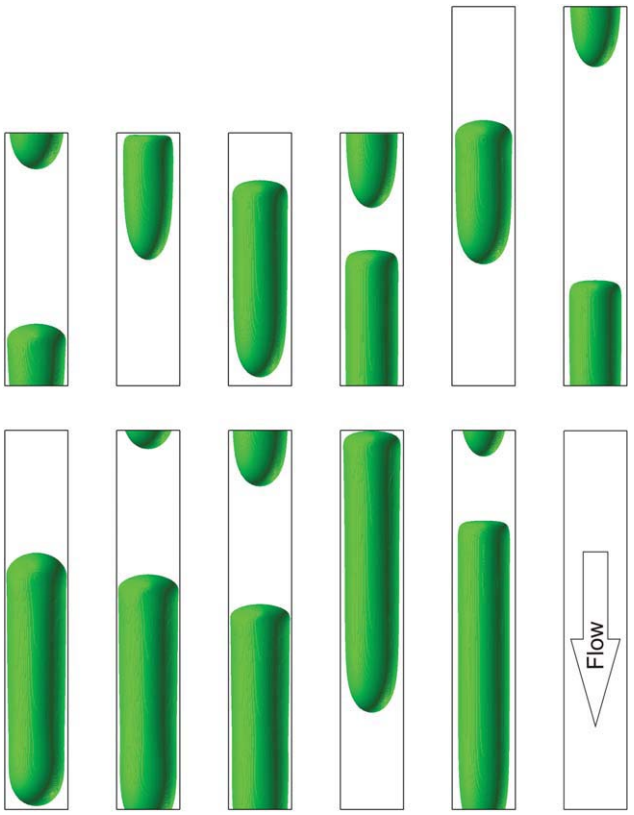

Figure 4. Lateral view of the three-dimensional bubble shape for all simulation runs.

With reference to Table 1, the figure shows from left to right cases 4_20_A, 4_20_B, 4_40_A, 4_40_B, 6_20_A, 6_20_B (top row) and 6_40_A, 6_40_B, 6_40_C, 6_40_D, 6_40_E (bottom row). [Color figure can be viewed in the online issue, which is available at www.interscience.wiley.com.]

quantified by the volume-equivalent bubble diameter, $D_{eq} \equiv (6V_B/\pi)^{1/3}$, where $V_B = \varepsilon_G L_{uc} W^2$. We note that for semi-infinite bubbles, the liquid film thickness, and thus the bubble diameter is independent of the bubble length.[29,30] Hence, for $D_{eq}/W \gg 1$ the ratio D_B/W should become independent of the bubble size and a function of Ca only. Kreutzer et al.[11] fitted data of experimental and numerical studies and proposed the following correlation for the bubble diameter in the diagonal direction of a square channel.

$$\frac{D_{B,diag}}{W} = 0.7 + 0.5\exp(-2.25Ca^{0.445}). \quad (1)$$

Since in the present simulations, the bubble shape is axisymmetric, we compared our numerical results for D_B with Eq. 1. Figure 5 shows that the bubble diameter obtained from our simulations was in general higher than suggested by Eq. 1.

For mass transfer applications the interfacial area per unit volume is of great importance. In Figure 6, we display the values of $a_i \equiv A_B/V_{uc}$ and $a_B \equiv A_B/V_B = a_i/\varepsilon_G$ as evaluated from the different simulations as functions of the capillary number. The interfacial area per volume of the unit cell a_i is, as expected, about two times higher for the cases with $\varepsilon_G = 0.4$ than for the cases with $\varepsilon_G = 0.2$. For the same value of ε_G, the values of a_i are slightly higher for the shorter unit

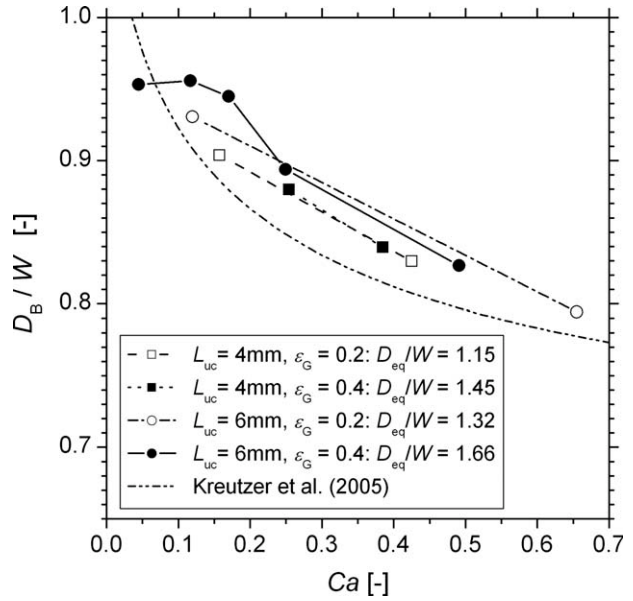

Figure 5. Bubble diameter vs. capillary number.

Comparison of simulation results with Eq. 1 from Kreutzer et al.[11]

cells. A comparison of all cases, for which the values of L_{uc} and ε_G are the same, shows that a_i increases slightly as the capillary number increases. The same trend is found for a_B. For a given capillary number, the value of a_B increases as ε_G and L_{uc}/W decreases. In general, larger values of a_B indicate a higher degree of deformation of the bubble from the spherical shape, although a_B also depends on D_{eq}. Based on the present numerical results, we propose the following correlation for the interfacial area per unit volume for co-current downward Taylor flow in a square mini-channel.

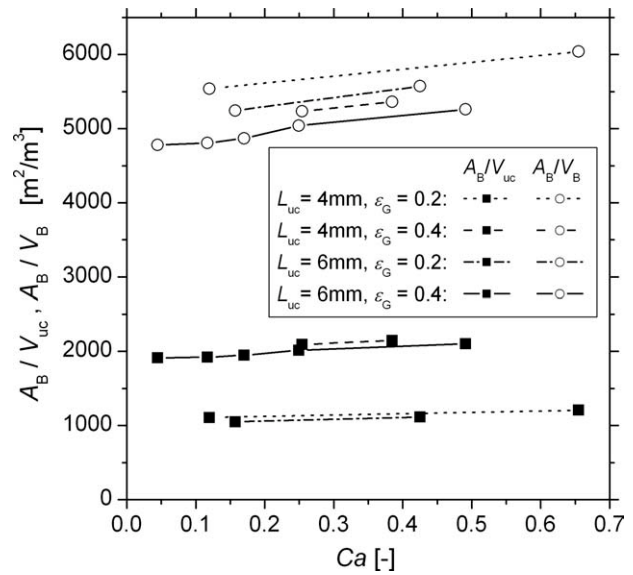

Figure 6. Simulation results for interfacial area per volume of the unit cell ($a_i = A_B/V_{uc}$) and interfacial area per bubble volume ($a_B = A_B/V_B$) as a function of the capillary number.

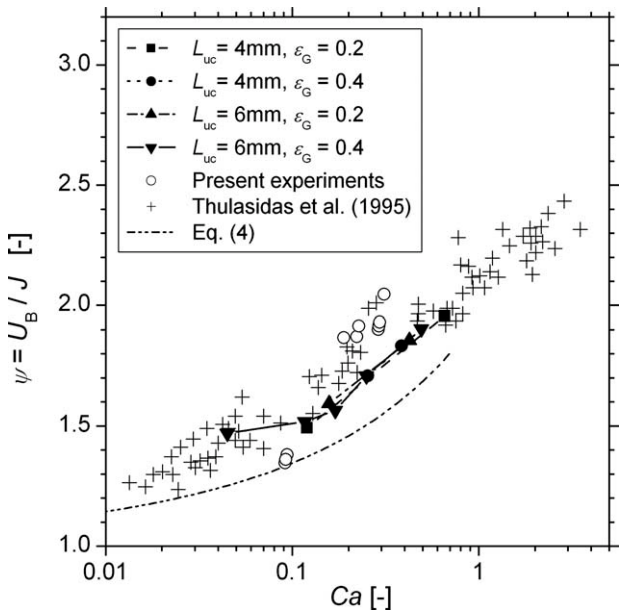

Figure 7. Ratio of bubble velocity to total superficial velocity vs. capillary number.

Comparison of the present experimental (open circles) and numerical results (filled symbols) with the experimental data of Thulasidas et al.[14] and Eq. 4 according to Liu et al.[32]

$$a_i = \frac{2.9\beta^{0.875}}{W}. \tag{2}$$

The maximum relative error of this correlation is 10%.

Influence of capillary number on bubble velocity

We now investigate the dependence of the bubble velocity on the capillary number. Here, we consider the flow of two incompressible phases through a straight channel with constant cross-section. From mass continuity it follows that the total volumetric flow rate at any axial position of the channel is equal to the total volumetric flow rate at the channel inlet.[31] Therefore, for Taylor flow it is $U_{sl} = J$, where U_{sl} is the mean axial velocity in the liquid slug.[31] Figure 7 displays the present numerical and experimental results for the velocity ratio $\psi \equiv U_B/J = U_B/U_{sl}$ as function of the capillary number. For the comparison only those experimental data are considered where the temporal variations of the bubble and slug length and the length of the unit cell are small. Since further experimental data are not available in literature for co-current downward flow, we additionally compare our results to those of two experiments for vertical co-current upward Taylor flow. Thulasidas et al.[14] considered the flow of air and silicon oil through a square mini-channel with 2 mm hydraulic diameter. Liu et al.[32] performed experiments in capillaries with circular and square cross-section with hydraulic diameter in the range of 0.9–3 mm using air and three different liquids. They fitted their experimental data by the correlation.

$$\frac{U_B}{J} = \frac{1}{1 - 0.61Ca_J^{0.33}}. \tag{3}$$

Equation 3 is valid for $2 \times 10^{-4} \leq Ca_J \leq 0.39$, where $Ca_J \equiv \mu_L J/\sigma = Ca/\psi$ is the capillary number based on the total superficial velocity. Equation 3 is equivalent to the following relation between ψ and Ca.

$$Ca \approx 4.47\frac{(\psi - 1)^3}{\psi^2}. \tag{4}$$

This relation, which is valid in the range of $2.08 \times 10^{-4} \leq Ca \leq 0.706$, is plotted in Figure 7. It can be seen that the present experimental and numerical results for co-current downward flow are in the same range as the experimental data for co-current upward flow. However, the present numerical results agree better with the data of Thulasidas et al.[14] than with the correlation of Liu et al.[32]

Relation between bubble velocity and total superficial velocity

In practical applications, the flow rates of the phases are often prescribed so that the superficial velocities J_L and J_G are given. Then, the total superficial velocity $J = J_L + L_G$ and the volumetric flow rate ratio $\beta \equiv J_G/J$ are known. Of interest are the resulting bubble velocity and the gas volume fraction of the Taylor flow. If either ε_G or U_B is known, then the other quantity can be computed from $J_G = \varepsilon_G U_B$. Thus, we require a relation between U_B and J, such as in Eq. 3, or a relation between ε_G and J. Knowing U_B or ε_G one can compute the capillary number and then determine the bubble diameter and the liquid film thickness. Conversely, these relations can be used to estimate suitable values for J_L and J_G to establish a certain value of the liquid film thickness.

In literature, two classical and closely related approaches exist to correlate the bubble velocity to the total superficial velocity. In the Nicklin equation,[33] this relation is given by

$$U_B = 1.2J + 0.35\sqrt{gD}, \tag{5}$$

while in the more general drift-flux model of Zuber and Findlay[34] it is

$$U_B = C_0 J + U_{G-J}. \tag{6}$$

Here, C_0 is the distribution parameter and U_{G-J} is the drift velocity. Thus, Eq. 5 is obtained from Eq. 6 by setting $C_0 = 1.2$ and by taking the drift velocity to be equal to the buoyant rise velocity of a bubble through a stagnant liquid in a tube of diameter D. The parameter C_0 is usually taken equal to the ratio between the maximum liquid velocity (at the axis) and the average liquid velocity, and then ranges from 1.2 for turbulent flow to approximately two for laminar flow in a pipe. For millimeter size channels, large variations of the values of C_0 and U_{G-J} are reported in the literature. Ide et al.[35] performed experiments for air–water flow in circular and rectangular capillaries with hydraulic diameter in the millimeter range. They found that the drift velocity is approximately zero, independent of the flow direction. Their experimental data are well correlated by $U_B = 1.2J$, both for circular and rectangular capillaries and for upward and downward flow. In other references C_0 varies from 0.85 to 1.38 (see the overview in Tsoligkas et al.[15]). The latter authors

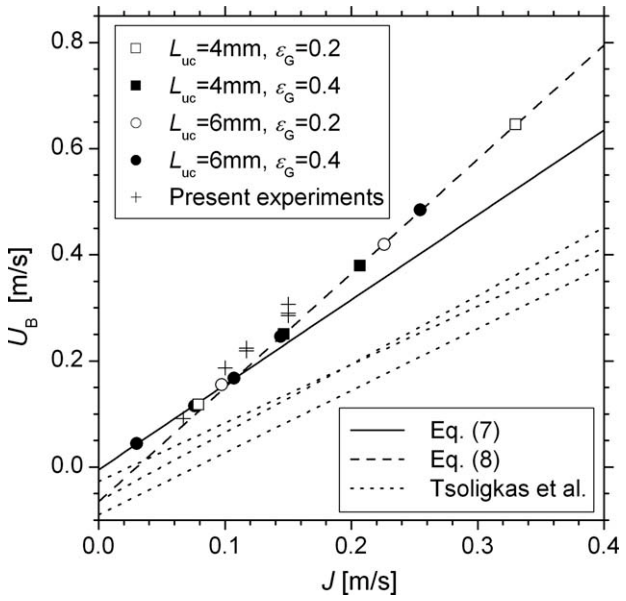

Figure 8. Comparison of present experimental (+) and numerical results (circles and squares) for bubble velocity vs. total superficial velocity, and approximation of the numerical results by the drift-flux model, Eqs. 7 and 8.

The dotted lines correspond to the fitting of the experimental data of Tsoligkas et al.[15] by the drift-flux model.

find that their experimental data for downward flow in a square channel ($W = 1.5$ mm and $W = 2$ mm) with two different liquid phases (water and an isopropanol–water mixture) can be fitted by three correlations where $1.1 \leq C_0 \leq 1.29$ and -0.0027 m/s $\leq U_{G-J} \leq -0.064$ m/s. Notably, U_{G-J} is nonzero and negative as the bubble velocity is taken as positive in the downward direction, and the bubbles would rise upwards due to buoyancy. In Figure 8, we compare our experimental and numerical results with the correlations of Tsoligkas et al.[15] For $J \leq 0.109$ m/s the present numerical data are well fitted by

$$U_B = 1.6J - 0.005 \text{ m/s}, \tag{7}$$

while for $J > 0.109$ m/s they are well fitted by

$$U_B = 2.15J - 0.065 \text{ m/s}. \tag{8}$$

Interestingly, there is no notable influence of the unit cell length and the gas holdup on C_0 and U_{G-J}. However, C_0 depends on the capillary number. This becomes apparent from Figure 7, where the ratio U_B/J is not constant but depends on Ca. On one hand side, Eqs. 7 and 8 indicate that for squalane the value of C_0 is much higher than for water. On the other side both correlations confirm the result of Tsoligkas et al.[15] that in downward flow U_{G-J} is nonzero and negative.

Relation between volumetric flow rate ratio and void fraction

In this section, we are interested in an equation that relates the unknown value of ε_G to a given value of β. We note that $\beta = \varepsilon_G U_B/J$ so that the ratio β/ε_G is equal to the ratio $U_B/J = U_B/U_{sl}$ which was investigated previously (see Figure 7). In Figure 9, we compare the values of ε_G and β from the present experiments and simulations with common correlations. The solid line corresponds to homogenous flow, where the phases move with the same velocity so that $\varepsilon_G = \beta$ and $U_{sl} = U_B$. The dashed line represents the Armand correlation[36] which was proposed for tubes of conventional size and is given by $\varepsilon_G = 0.833\beta$. From a recent experiment[37] in a glass microchannel of rectangular cross-section (100 μm $\times$ 50 μm) it was reported that the gas holdup in nitrogen/water Taylor flow follows the Armand correlation. In that experiment U_B was varied between 0.24 and 7.12 m/s leading to capillary numbers in the range of 0.003–0.1 and bubble Reynolds numbers in the range of 20–700. The validity of the Armand correlation implies that the liquid film thickness (which was not measured in that experiment) is not a function of the bubble velocity. In the present study, we have much lower bubble Reynolds numbers and find a clear dependence of the liquid film thickness (and bubble diameter) on the bubble velocity (and Ca) and the Armand correlation is not valid. The Armand correlation corresponds to a constant ratio $\varepsilon_G/\beta = U_{sl}/U_B = 0.833$. In the present experiments and simulations, we always have $\varepsilon_G/\beta = U_{sl}/U_B < 0.833$ as shown in Figure 9. In particular, we observe from the numerical simulations that these ratios depend on the capillary number (see also Figure 7). With the increasing values of Ca the ratios $\varepsilon_G/\beta = U_{sl}/U_B$ are decreasing, i.e., the difference between the bubble velocity and the mean velocity in the liquid slug is increasing. This behavior is reasonable, because the bubble diameter D_B decreases with

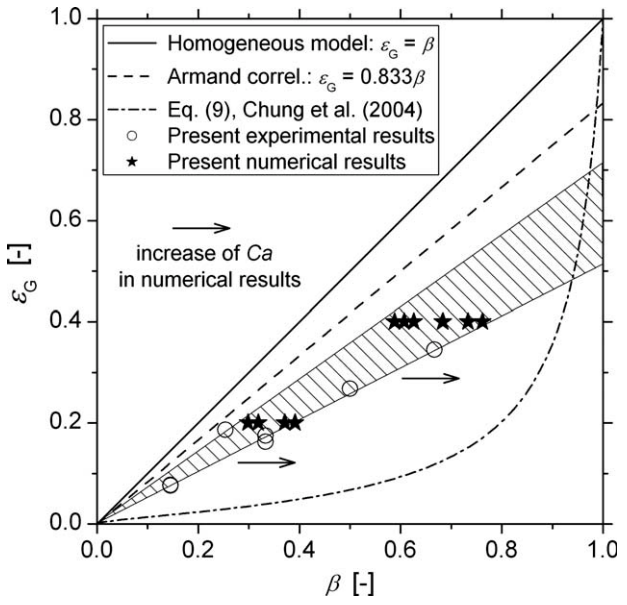

Figure 9. Gas holdup in the unit cell vs. volumetric flow rate ratio.

Comparison of the present experimental and numerical results with the homogeneous model, the Armand correlation[36] and Eq. 9 of Chung et al.[38] The arrows indicate an increase of Ca in the simulations while the two lines enclosing the shaded area correspond to the fitting of the numerical data in Figure 8 by Eqs. 7 and 8, respectively.

increasing value of Ca (see Figure 5) and thus the bubble occupies a region in the cross-section of the duct with higher average velocity.

Chung et al.[38] found that their data for water–nitrogen flow in a 100-μm circular channel and a 96-μm square channel are fitted well by the relation

$$\varepsilon_G = \frac{C_1 \beta^{0.5}}{1 - C_2 \beta^{0.5}}, \tag{9}$$

where $C_1 = 0.03$ and $C_2 = 0.97$ are constants determined from their experiment. Figure 9 shows that for low Ca our numerical data are closer to the Armand correlation, while they shift toward Eq. 9 for larger Ca. We note that Eq. 6 can be recast to give the following relation between ε_G and β.

$$\varepsilon_G = \frac{\beta}{C_0 + U_{G-J}/J}. \tag{10}$$

This shows that for $U_{G-J} \neq 0$ the gas holdup does not only depend on β but also on J. The maximum value of J in the present simulations is 0.34 m/s. The corresponding value of U_{G-J} is 0.065 m/s, according to Eq. 8. Introducing both values in Eq. 10 and setting C_0 to 1.6 and 2.15 according to Eqs. 7 and 8 yields two straight lines. These two lines enclose the shaded area in Figure 9. This area roughly defines the parameter space with respect to ε_G and β that can be realized for co-current downward Taylor flow of squalane and nitrogen in a square mini-channel with 1-mm hydraulic diameter for $L_{uc} \leq 6$ mm.

Conclusions

In the present paper, a series of VOF simulations of the co-current downward Taylor flow of squalane and nitrogen in a square channel with 1-mm hydraulic diameter were performed. For the verification of the in-house computer code, the computed bubble shapes were compared with the experimental flow visualizations, and a good agreement for different values of the capillary number was obtained. From the present numerical results, where the bubble shape is axisymmetric and where the capillary number and bubble Reynolds number are in the range of $0.045 \leq Ca \leq 0.66$ and $1.22 \leq Re \leq 17.9$, respectively, the following conclusions can be drawn:

With the increasing capillary number, the liquid film thickness increases and the bubble diameter decreases. The curvature of the front meniscus increases with increasing Ca while that of the back meniscus decreases. The interfacial area per unit volume a_i slightly increases with increasing Ca for a fixed gas holdup ε_G. For a_i, a power law correlation in terms of the volumetric flow rate ratio β is proposed in Eq. 2 that approximates the numerical results with an error of $<10\%$.

The ratio between bubble velocity U_B and total superficial velocity J increases with the increase of Ca and is in the same range as experimental data for co-current upward flow. The relation between U_B and J can be described by a drift-flux model, with different values for the distribution coefficient C_0 and the drift velocity U_{G-J} for values of J smaller and larger than 0.109 m/s (see Eqs. 7 and 8). The values of the distribution coefficient are rather large ($C_0 = 1.6$ and $C_0 = 2.15$), while the values for the drift velocities are negative for downward flow.

It is found that the relation between ε_G and β cannot be described by a linear relationship, such as the homogeneous model or the Armand correlation. For the same value of ε_G, different values of β were obtained for different values of Ca. Therefore, improved correlations should be developed which take into account the capillary number Ca_J, which is based on the total superficial velocity as velocity scale.

Notation

A_B = bubble interfacial area, m^2
a_i = interfacial area per volume of the unit cell, 1/m
a_B = interfacial area per bubble volume, 1/m
C_0 = distribution coefficient in drift-flux model
Ca = capillary number, $Ca \equiv \mu_L U_B/\sigma$
Ca_J = capillary number based on velocity J, $Ca_J \equiv \mu_L J/\sigma$
D = pipe diameter, m
D_B = bubble diameter, m
D_{eq} = volume-equivalent diameter, m
D_h = hydraulic diameter, m
Eo = Eötvös number, $Eo \equiv g(\rho_L - \rho_G)D_h^2/\sigma$
g = gravitational acceleration, m/s^2
h = mesh width, m
J = total superficial velocity, $J \equiv J_G + J_L$, m/s
J_G = gas superficial velocity, m/s
J_L = liquid superficial velocity, m/s
J_{uc} = axial length of the unit cell, m
L_x, L_y, L_z = dimensions of the computational domain, m
La = Laplace number, $La \equiv \sigma \rho_L D_h/\mu_L^2$
Δp = pressure difference across the unit cell, Pa
Re_B = bubble Reynolds number, $Re_B \equiv \rho_L D_h U_B/\mu_L$
U_B = bubble velocity, m/s
U_{G-J} = drift velocity in drift-flux model, m/s
U_{sl} = mean axial velocity in the liquid slug, m/s
V_B = bubble volume, m^3
W = inner side length of square channel, m
We = Weber number, $We \equiv \rho_L D_h U_B^2/\sigma$
x, y, z = Cartesian co-ordinates, m

Greek letters

β = volumetric flow rate ratio, $\beta \equiv J_G/J$
δ_{LF} = liquid film thickness, m
ε_G = gas hold-up
Λ = Laplace length, m
μ = viscosity, Pa s
ψ = nondimensional bubble velocity, $\psi \equiv U_B/J$
ρ = density, kg/m^3
σ = coefficient of surface tension, N/m

Subscripts

B = bubble
G = gas phase
L = liquid phase
sl = slug
uc = unit cell

Literature Cited

1. Roy S, Bauer T, Al-Dahhan M, Lehner P, Turek T. Monoliths as multiphase reactors: a review. *AIChE J*. 2004;50:2918–2938.
2. Hessel V, Angeli P, Gavriilidis A, Löwe H. Gas–liquid and gas–liquid–solid microstructured reactors: contacting principles and applications. *Ind Eng Chem Res*. 2005;44:9750–9769.
3. Irandoust S, Andersson B. Liquid film in Taylor flow through a capillary. *Ind Eng Chem Res*. 1989;28:1684–1688.

4. Davies RM, Taylor GI. The mechanics of large bubbles rising through extended liquids and through liquids in tubes. *Proc R Soc London Ser A*. 1950;200:375–390.
5. Edvinsson Albers R, Nyström M, Siverström M, Sellin A, Dellve AC, Andersson U, Herrmann W, Berglin T. Development of a monolith-based process for H_2O_2 production: from idea to large-scale implementation. *Catal Today*. 2001;69:247–252.
6. De Deugd RM, Chougule RB, Kreutzer MT, Meeuse FM, Grievink J, Kapteijn F, Moulijn JA. Is a monolithic loop reactor a viable option for Fischer-Tropsch synthesis? *Chem Eng Sci*. 2003;58:583–591.
7. Güttel R, Kunz U, Turek T. Reactors for Fischer-Tropsch synthesis. *Chem Eng Technol*. 2008;31:746–754.
8. Guettel R, Knochen J, Kunz U, Kassing M, Turek T. Preparation and catalytic evaluation of cobalt based monolithic and powder catalysts for Fischer-Tropsch synthesis. *Ind Eng Chem Res*. 2008;47:6589–6597.
9. Liu W, Hu J, Wang Y. Fischer-Tropsch synthesis on ceramic monolith-structured catalysts. *Catal Today*. 2009;140:142–148.
10. Pangakar K, Schildhauer TJ, van Ommen R, Nijenhuis J, Kapteijn F, Moulijn JA. Structured packings for multiphase catalytic reactors. *Ind Eng Chem Res*. 2008;47:3720–3751.
11. Kreutzer MT, Kapteijn F, Moulijn JA, Heiszwolf JJ. Multiphase monolith reactors: chemical reaction engineering of segmented flow in microchannels. *Chem Eng Sci*. 2005;60:5895–5916.
12. Angeli P, Gavriilidis A. Hydrodynamics of Taylor flow in small channels: a review. *J Mech Eng Sci*. 2008;222:737–751.
13. Mantle MD, Sederman AJ, Gladden LF, Raymahasay S, Winterbottom JM, Stitt EH. Dynamic MRI visualization of two-phase flow in a ceramic monolith. *AIChE J*. 2002;48:909–912.
14. Thulasidas TC, Abraham MA, Cerro RL. Bubble-train flow in capillaries of circular and square cross-section. *Chem Eng Sci*. 1995;50:183–199.
15. Tsoligkas AN, Simmons MJH, Wood J. Influence of orientation upon the hydrodynamics of gas–liquid flow for square channels in monolith supports. *Chem Eng Sci*. 2007;62:4365–4378.
16. Tsoligkas AN, Simmons MJH, Wood J. The Effect of Hydrodynamics on the Reaction Rates in Capillary Reactor. Leipzig, Germany: 6th International Conference on Multiphase Flow, CD-ROM, 2007.
17. Ghidersa B, Wörner M, Cacuci DG. Exploring the flow of immiscible fluids in a square vertical mini-channel by direct numerical simulation. *Chem Eng J*. 2004;101:285–294.
18. Taha T, Cui ZF. CFD modelling of slug flow inside square capillaries. *Chem Eng Sci*. 2006;61:665–675.
19. Wörner M, Ghidersa B, Onea A. A model for the residence time distribution of bubble-train flow in a square mini-channel based on direct numerical simulation results. *Int J Heat Fluid Flow* 2007;28:83–94.
20. Liu D, Wang S. Hydrodynamics of Taylor flow in noncircular capillaries. *Chem Eng Process*. 2008;47:2098–2106.
21. Onea A, Wörner M, Cacuci DG. A qualitative computational study of mass transfer in upward bubble train flow through square and rectangular mini-channels. *Chem Eng Sci*. 2009;64:1416–1435.
22. Ndinisa NV, Wiley DE, Fletcher DF. Computational fluid dynamics simulations of Taylor bubbles in tubular membranes: model validation and application to laminar flow systems. *Chem Eng Res Des*. 2005;83:40–49.
23. Özkan F, Wörner M, Wenka A, Soyhan HS. Critical evaluation of CFD codes for interfacial simulation of bubble-train flow in a narrow channel. *Int J Numer Methods Fluids*. 2007;55:537–564.
24. Claeys M. Selektivität, Elementarschritte und Kinetische Modellierung bei der Fischer-Tropsch-Synthese. PhD Thesis, University Karlsruhe, Karlsruhe, Germany, 1997.
25. Bauer T. Experimental and Theoretical Investigations of Monolithic Reactors for Three-Phase Catalytic Reactions. PhD Thesis, Technical University Dresden, Dresden, Germany, 2007.
26. Öztaskin MC, Wörner M, Soyhan HS. Numerical investigation of the stability of bubble train flow in a square mini-channel. *Phys Fluids*. 2009;21:042108.
27. Ratulowski J, Chang HS. Transport of gas bubbles in capillaries. *Phys Fluids*. 1989;A1:1642–1655.
28. Martinez MJ, Udell KS. Boundary integral analysis of the creeping flow of long bubbles in capillaries. *J Appl Mech*. 1989;56:211–217.
29. Bretherton FB. The motion of long bubbles in tubes. *J Fluid Mech*. 1961;10:166–188.
30. Hazel AL, Heil M. The steady propagation of a semi-infinite bubble into a tube of elliptical or rectangular cross-section. *J Fluid Mech*. 2002;470:91–114.
31. Suo M, Griffith P. Two-phase flow in capillary tubes. *ASME J Basic Eng*. 1964;86:576–582.
32. Liu H, Vandu CO, Krishna R. Hydrodynamics of Taylor flow in vertical capillaries: flow regimes, bubble rise velocity, liquid slug length, and pressure drop. *Ind Eng Chem Res*. 2005;44:4884–4897.
33. Nicklin DJ, Wilkes JO, Davidson JF. Two-phase flow in vertical tubes. *Trans Inst Chem Eng*. 1962;40:61–68.
34. Zuber N, Findlay JA. Average volumetric concentration in two-phase flow systems. *J Heat Transfer*. 1965;78:453–468.
35. Ide H, Kariyasaki A, Fukano T. Fundamental data on the gas–liquid two-phase flow in minichannels. *Int J Therm Sci*. 2007;46:519–530.
36. Armand AA, Treschew GG. The resistance during the movement of a two-phase systems in horizontal pipe. *Izv Vses Teplotek Inst*. 1946;1:16–23.
37. Warnier MJF, Rebrov EV, de Croon MHJM, Hessel V, Schouten JC. Gas hold-up and liquid film thickness in Taylor flow in rectangular microchannels. *Chem Eng J*. 2008;135S:S153–S158.
38. Chung PMY, Kawaji M, Kawahara A, Shibita Y. Two-phase flow through square and circular microchannels—effects of channel geometry. *J Fluids Eng*. 2004;126:546–552.

Manuscript received Jan. 28, 2009, and revision received Sep. 23, 2009.